Int. J. Electrochem. Sci., 13 **(2018)** 7800 – 7815, doi: 10.20964/2018.08.51

International Journal of
ELECTROCHEMICAL
SCIENCE
www.electrochemsci.org

Effect of Laser Remelting on Microstructure and Electrochemical Corrosion of S355 Structural Steel

*Chen Haixiang, Kong Dejun**

School of Mechanical Engineering, Changzhou University, Changzhou 213164, P.R. China
*E–mail: kong–dejun@163.com

Received: 9 May 2018 / *Accepted:* 19 June 2018 / *Published:* 5 July 2018

A S355 structural steel was processed using a laser remelting (LR) at laser powers of 1000, 1300 and 1500 W. The surface and cross–section morphologies, distributions of chemical elements, phase compositions, residual stresses and crystallization transition temperatures of as–obtained remelted layers were analyzed using a scanning electron microscope (SEM), energy–dispersive spectrometer (EDS), X–ray diffractometer (XRD), X–ray diffraction stress tester, and differential scanning calorimetry (DSC), respectively. The polarization curves and AC impedances of remelted layers in 3.5% NaCl solution were tested using a CHI660E type electrochemical workstation to investigate the effects of LR on their corrosion behaviors. The results show that the surface roughness of remelted layers decrease with the laser powers increasing, the Mn, Cr, Si and O form the atoms–rich zones on the remelted layers at the laser powers of 1000 and 1300 W, while the Fe forms the atom–poor zones on the remelted layers. The remelted layers are mainly composed of Fe_2MoO_4, $MnFe_2O_4$, $NiMn_2O_4$, and $MnCr_2O_4$, and with a certain amount of amorphous structure. The residual stress of remelted layers at laser power of 1000 W is 64.4 ± 9 MPa, which decreases its electrochemical corrosion resistance, while that at laser powers of 1300 and 1500 W is –2.3 ± 13, and –63.3 ± 9 MPa, respectively, which increase their electrochemical corrosion resistance. The corrosion potential of remelted layers at laser powers of 1000, 1300, and 1500 W is –0.502, –0.49, and –0.472 V, respectively, and the corresponding charge transfer resistances is 1807, 1585, and 1672 $\Omega \cdot cm^2$, respectively, showing that the corrosion resistance of S355 steel is increased by LR.

Keywords: S355 steel; laser remelting (LR); surface and cross–section morphology; differential scanning calorimetry (DSC); residual stress; electrochemical corrosion

1. INTRODUCTION

As a low–alloy structural steel, S355 steel is widely used in important bearing components on offshore platforms owing to its high strength, low temperature impact toughness and excellent weldability [1]. However, S355 steel easily produces electrochemical corrosion in marine environment

[2, 3]. In seawater, Fe is acted as the anode and undergoes the oxidation process, the cathode has reduction process: $2H^+ + 2e^- \rightarrow H_2$, seawater is acted as an electrolyte, which serves as an electron transfer medium using ion [4], causing S355 steel subjected to be corroded by primary battery [5]. In addition, the inclusions in S355 steel also create an electrochemical potential difference between the inclusions and the substrate, causing the inclusion site more susceptible to localized corrosion attack [6], which drastically reduced its mechanical properties and service life. Fortunately, surface modification treatment is an effective method to improve the surface properties of S355 steel. Laser remelting (LR) is a new method of surface modification technology with no additional materials, a certain thickness of S355 steel can be remelted and resolidified (10^5–10^8 K/s) quickly [7], which releases the internal impurities in a certain depth to reduce the inclusions and achieve uniform microstructure [8–10], therefore, LR is an effective way to increase its electrochemical corrosion resistance [11]. Compared to other surface treatments, LR is a cost–effective method without changing the chemical compositions, which does not select the materials of remelted layer and explore complex process parameters [11]. At the same time, LR is a non–equilibrium process of local rapid solidification, and a part of amorphous structure can be obtained by high cooling rate. The amorphous structure exhibits good corrosion resistance due to lack of grain boundary, dislocation and other structural defects [12].

At present, LR has attracted wide attention on the microstructure and properties of alloy steel [13], Chikarakara et al [14] researched the effects of LR on the microstructure of AISI 316L stainless steel; Zhang et al [15] investigated the effects of LR on the wear resistance of AZ91D magnesium alloy; Yao et al [9] discussed the effects of LR on microstructure and mechanical properties of Ti–Ni beta titanium alloy; Zhang et al [16] studied the microstructure, hardness and thermal fatigue properties of H21 steel by LR. However, there are few reports about laser remelted S355 structural steel. Therefore, it is crucial to investigate the effects of LR on its microstructure and electrochemical corrosion.

As a direct representation of heat input, laser power has an important effect on the surface quality and properties of remelted layer [17]. The steel surface is difficult to be remelted completely by the insufficient laser power, failing to eliminate the internal impurities in steel and holes would rise to steel surface, forming pores. Conversely, the excessive laser power will over–burnt the steel surface seriously. Therefore, it is significant to explore the effects of laser power on the microstructure and electrochemical corrosion performances. In this study, a S355 steel was processed using a LR at the laser powers of 1000, 1300 and 1500 W. The surface and cross–section morphologies, phase compositions, element distributions and residual stresses were investigated to evaluate its electrochemical corrosion behaviors in 3.5% NaCl solution.

2. EXPERIMENTAL

The substrate material was the European standard S355 structural steel, its mass fraction of chemical elements (wt, %): C 0.17, Si 0.55, Mn 0.94, P 0.035, Cr 0.065, S 0.035, Ni 0.065. Mo 0.30 and Zr 0.15, the rest was Fe. The LR test was conducted on a ZKSX–2000W type fiber–coupled laser spraying system, respective power of 1000, 1300 and 1500 W, Ar gas as protection gas. The process parameters of LR are shown in Table 1.

Table 1. Technological parameters of LR.

Item	Parameter
Laser power/W	1000/1300/1500
Scanning speed/mm/s	15
Spot diameter/mm	3
Spacing/mm	250
Overlap ratio/%	50
Argon gas speed/L/min	10

After the LR test, the morphologies and distributions of chemical elements of remelted layer surfaces and cross–sections were analyzed using a SUPRA55 field emission scanning electron microscope (FESEM) and its configured energy dispersive spectrometer (EDS), respectively, and their phases were analyzed using a D/max2500PC type X–ray diffractometer (XRD). The residual stresses of remelted layers were analyzed using an X350–A type stress tester with the method of inclination fixed 2φ, technogical parameters: fixed peak of cross–correlation function with Cu target–Kα radiation, Prague diffraction crystal face of 422, respective φ of 0, 15, 25, and 35 ^{o}, scanning angle 2θ of 151–162^{o}, stress constant of –179 MPa/^{o}, 2θ scan step distance of 0.1 ^{o}, counting time of 0.5 s, X–ray tube voltage of 20 kV, and X–ray tube current of 5 mA. The crystallization process of remelted layer was analyzed using a differential scanning calorimetry (DSC) in a crucible, the heating rang was 40–500 ^{o}C at the rate of 15 K/min, and the sample was heated to the required temperature under the protection of Ar. The polarization curves and AC impedance test were carried out on a CHI660E type electrochemical workstation. The three electrode system was used with the area of 10×10 cm^2 as the working electrode, the other surfaces were coated with epoxy resin. The platinum electrode was used as the auxiliary electrode, and the saturated calomel (SCE) as the reference electrode. Before the electrochemical testing, the sample surface was cleaned by the ultrasonic wave for 5 min, the thermostat was kept at 27 ^{o}C. The corrosion medium was 3.5% NaCl solution and the open circuit potential was measured for 600 s. The potentiodynamic polarization curves were measured at the potential range of –0.8 to –0.2 V, scanning rate of 0.001 V/s, quiet time of 2 s, sensitivity of $1 \times 10^{-0.002}$, and test time of 1000 s. Open circuit potential before the electrochemical impedance spectroscopy (EIS) was also measured for 10 min in order to reach steady state before the impedance measurement. The EIS was acquired at different applied potentials in the frequency range from 100 kHz to 0.01 Hz with the amplitude of 0.01 V in wave generated by a frequency response analyzer.

3. RESULTS AND DISCUSSION

3.1 Plane scan analysis of remelted layer surface

The plane scanned position of remelted layer surface at the laser power of 1000 W is shown in

Fig.1 (a). The remelted layer surface was rough and uneven. In the LR process, the input laser energy had an important influence on the temperature gradient. Low energy led to the short existence of molten pool and produced a steep temperature gradient from the molten pool center to edge [18]. The surface tension difference resulting from temperature gradient led to the net flow from the inner of molten pool to outer, causing the sag of molten pool center surface and bulge toward the periphery of molten pool [19]. In addition, the inconsistency of expansion and contraction in remelted layer caused the local surface difficult to keep flat. Before the melting pool reaching the height balance, the solidification intervened and formed the concave and convex surface [20]. The plane scan result is shown in Fig.1 (b). The remelted layer was mainly composed of Fe and Mn. A small amount of Si originated from the substrate, while the O was due to the high temperature oxidation during the LR test. The Fe, Mn, Si, and O were uniformly distributed on the remelted layer surface, as shown in Fig.1 (c)–(f).

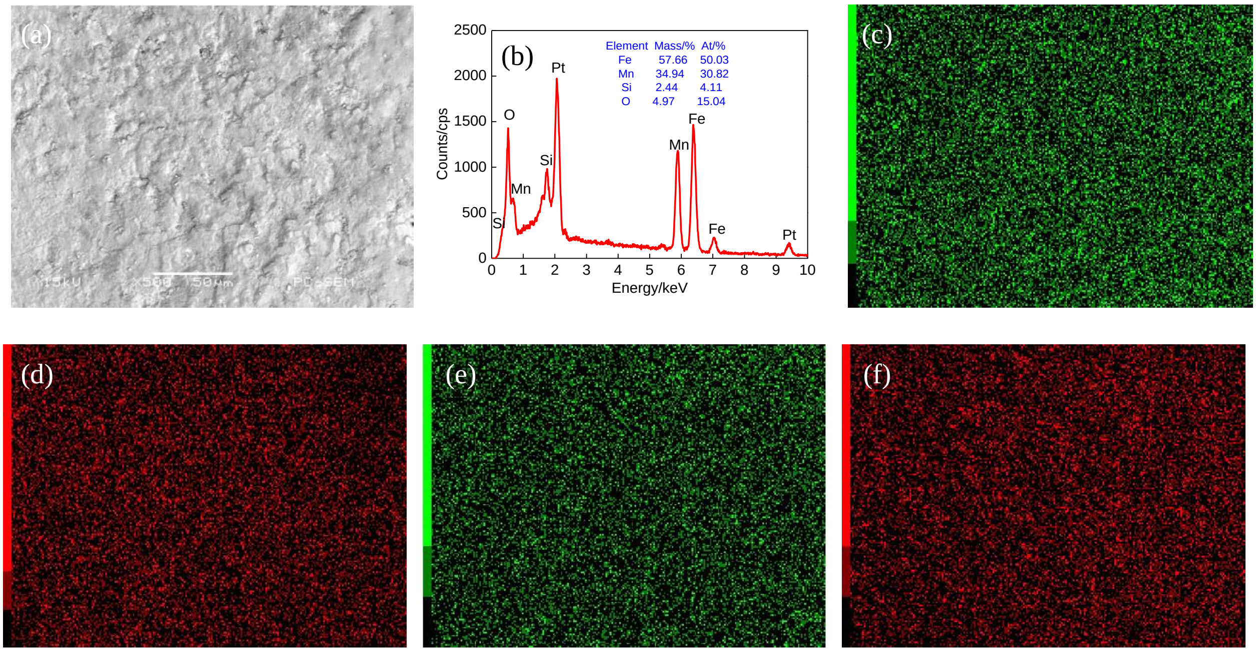

Figure 1. Plane scan analysis of remelted layer at laser power of 1000 W (a) Plane scanned position, (b) Result of plane scan analysis, (c) Fe content, (d) Mn content, (e) Si content and (f) O content

The plane scanned position of remelted layer at the laser power of 1300 W is shown in Fig. 2 (a). The uneven surface was slightly reduced compared that at the laser power of 1000 W. Generally, an increasing laser energy input reduced the melt viscosity and surface tension, promoting the liquid metal flow on molten pool surface [21]. The plane scan result is shown in Fig. 2 (b). The Fe and Mn were still the main constituent elements of remelted layer, the Fe content increased while the Mn content decreased compared to the remelted layer at the laser power of 1000 W. A small mount of Fe and O were also detected, there were no obvious atom–rich zones, which were uniformly distributed on the remelted layer, as shown in Fig. 2 (c) and (f). The distributions of Mn and Si were concentrated, there were the atoms–rich zones, as shown in Fig. 2 (d)–(e).

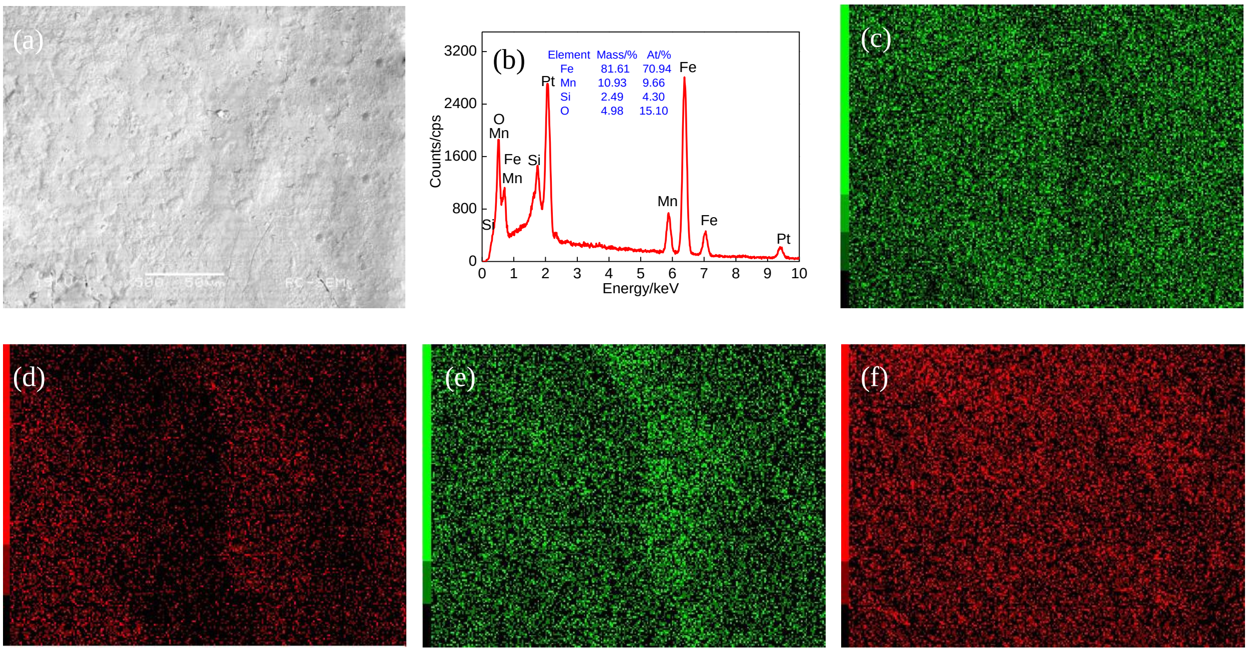

Figure 2. Plane scan analysis of remelted layer at laser power of 1300 W (a) Plane scanned position, (b) Result of plane scan analysis, (c) Fe content, (d) Mn content, (e) Si content and (f) O content

The plane scanned position of remelted layer at the laser power of 1500 W is shown in Fig. 3 (a). The remelted layer surface was more flat and smooth with the laser power further increasing, which was due to the higher laser power remelting and resolidifying the original surface completely. The more energy was absorbed by the original surface when the laser power was enough, leading to the microstructure of remelted zone tend to high uniformity [22]. Therefore, the microstructure was refined and compact, eliminating the most of micro–defects. The plane scan result is shown in Fig. 3 (b). The Fe content decreased while the Mn content increased compared to that at the laser power of 1300 W, a small amount of Si and O were still detected. The Fe, Mn and O were evenly distributed, as shown in Fig. 3 (c), (d) and (f), while the Si was inhomogeneously distributed and formed the atom–rich zones, as shown in Fig. 3 (e).

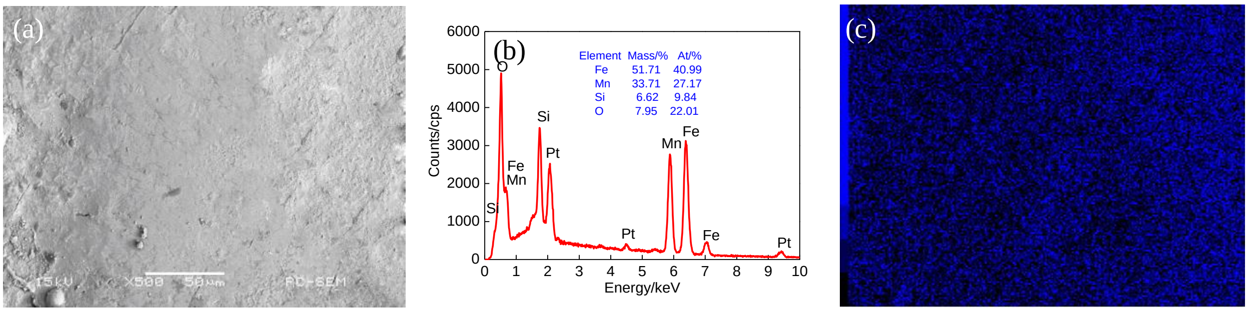

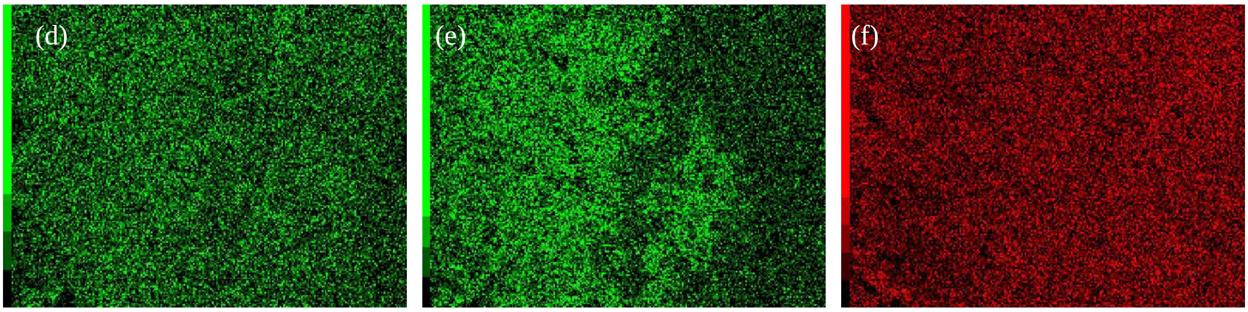

Figure 3. Plane scan analysis of remelted layer at laser power of 1500 W (a) Plane scanned position, (b) Result of plane scan analysis, (c) Fe content, (d) Mn content, (e) Si content and (f) O content

3.2 Plane scan analysis of cross–sections

The plane scanned position of remelted layer cross–section at the laser power of 1000 W is shown in Fig. 4 (a). The demarcation line between the remelted layer and the substrate was clearly visible. The thickness of remelted layer was macroscopically uniform but the microscopically roughness. The present of microcracks was due to the residual stress of solidification by LR. The Fe was obviously stratified and enriched in the substrate, as shown in Fig. 4 (b). The Mn, Cr, Si and O were enriched in the remelted layer, as shown in Fig. 4 (c)–(f).

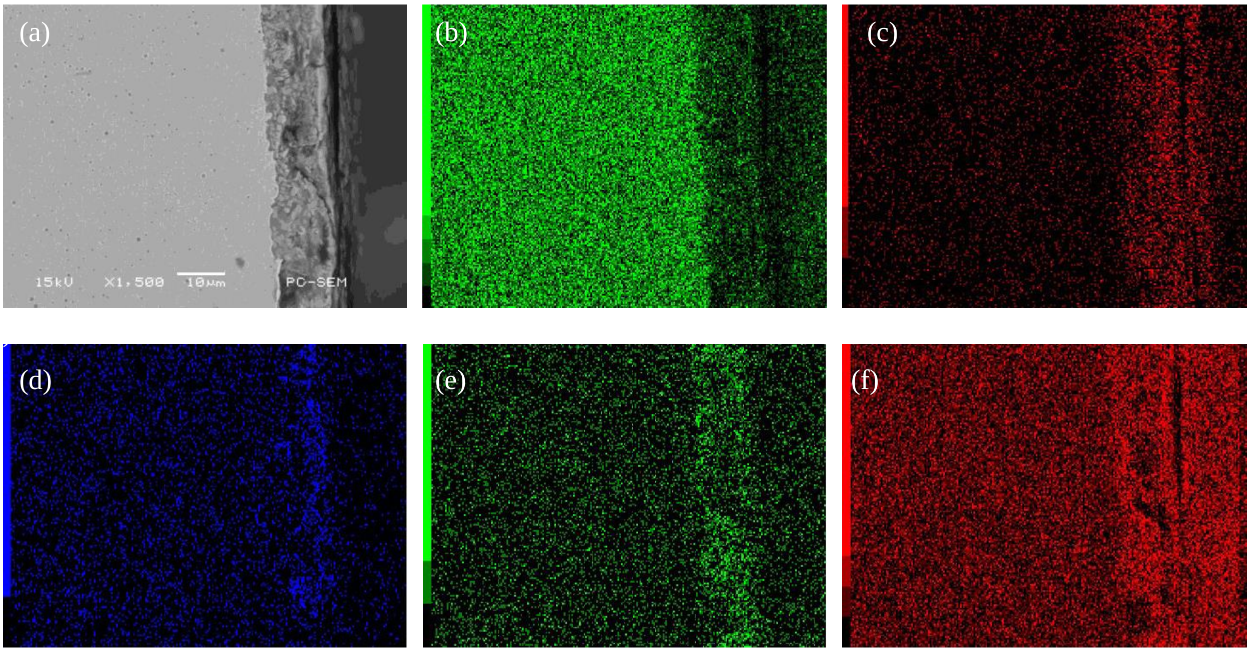

Figure 4. Plane scan analysis of remelted layer cross–section at laser power of 1000 W (a) Plane scanned position, (b) Fe content, (c) Mn content, (d) Cr content, (e) Si content and (f) O content

The plane scanned position of remelted layer cross–section at the laser power of 1300 W is shown in Fig. 5 (a). The thickness of remelted layer was uneven, there was pores on the remelted layer. This was because gases had no enough time to escape from the remelted layer surface and formed the pores. The Fe was enriched in the substrate, while the Mn, Cr, Si and O were enriched in the remelted layer, as shown in Fig. 5 (b)–(e).

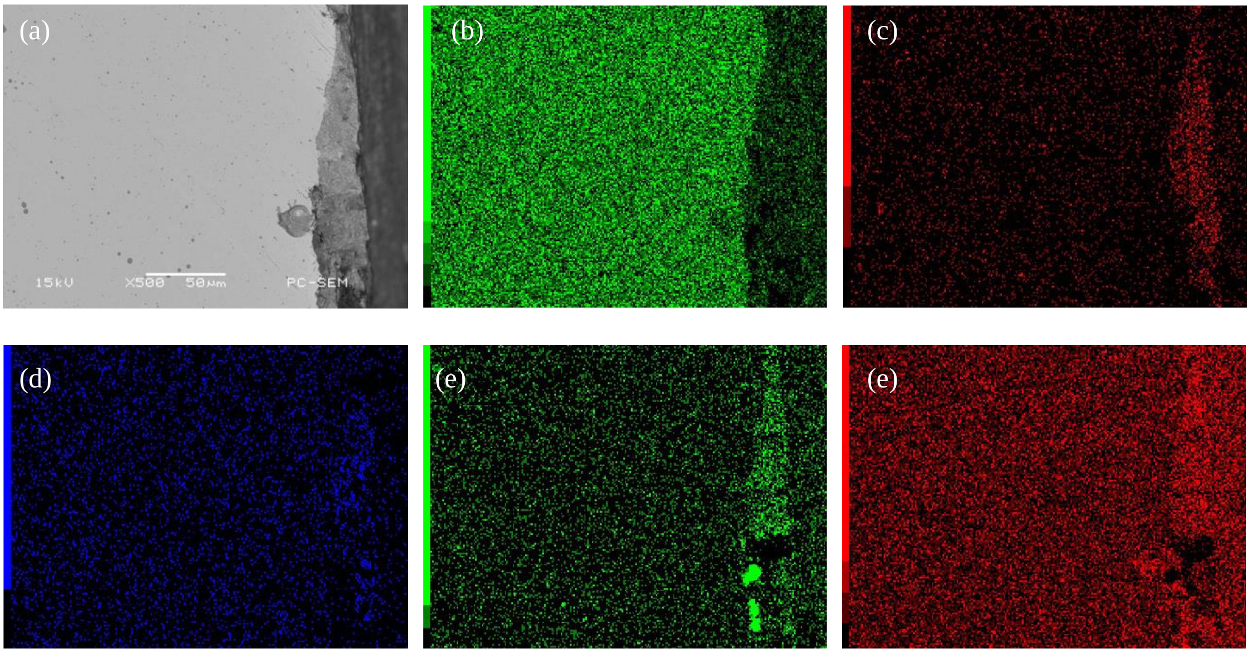

Figure 5. Plane scan analysis of remelted layer cross–section at laser power of 1300 W (a) Plane scanned position, (b) Fe content, (c) Mn content, (c) Cr content, (d) Si content and (e) O content

The plane scanned position of remelted layer cross–section at the laser power of 1500 W is shown in Fig. 6 (a). The bonding interface between the remelted layer and the substrate were also clearly visible, some pores appeared on the substrate cross–section due to the defects in the rolling process of S355. The main reason for the formation of bubbles in the remelted layer cross–section was that the metal vapor was ejected from the molten pool surface to form a vapor eddy during the LR test, the Ar and a small amount of air were involved in the molten pool. The mixed gases remained on the remelted layer due to the rapid cooling and solidifying of LR [23]. With the laser powers further increasing, the Fe was still barren on the remelted layer cross–section, while the Mn, Cr and Si were uniformly distributed, the atoms–rich zones disappeared, as shown in Fig. 6 (b)–(e). The O was still enriched due to high temperature oxidation during the LR test, as shown in Fig. 6 (f).

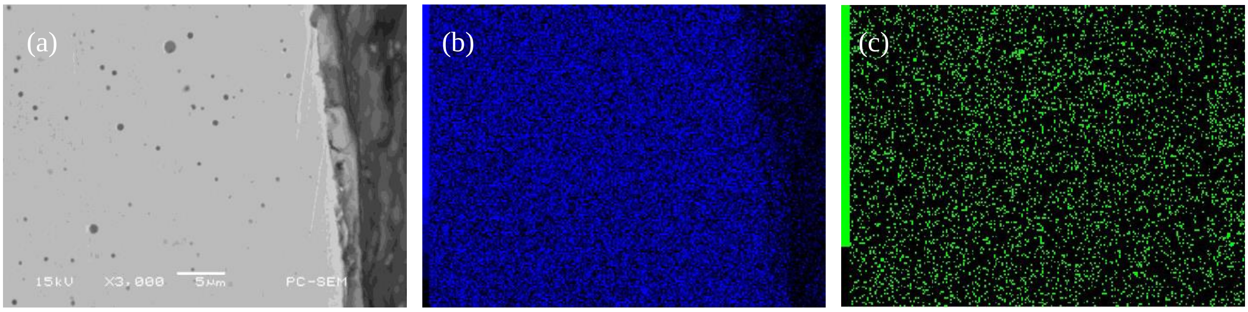

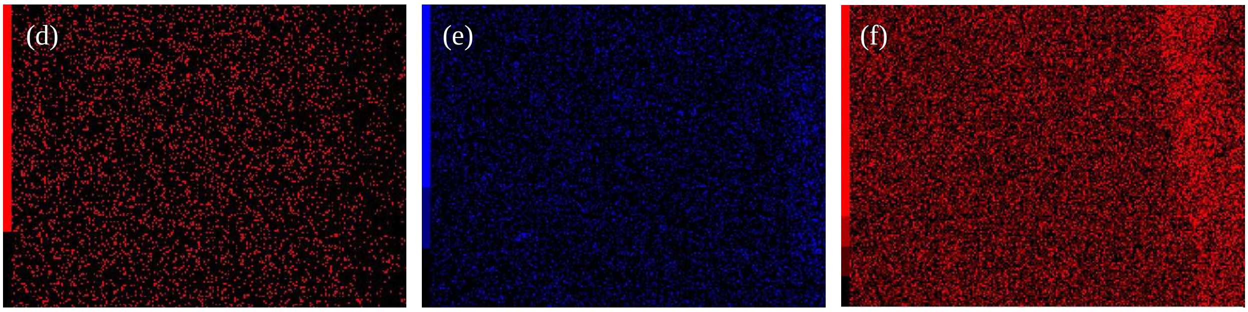

Figure 6. Plane scan analysis of remelted layer cross–section at laser power of 1500 W (a) Plane scanned position, (b) Fe content, (c) Mn content, (d) Cr content, (e) Si content and (f) O content

3.3 Line scan analysis of remelted layer cross–sections

The line scan analysis of remelted layer cross–section in Fig. 4 (a) is shown in Fig. 7. The Fe content revealed a gradient descent in the diffusion layer, as shown in Fig. 7 (a). The Mn rose in a gradient along the substrate to the remelted layer, and was obviously enriched in the remelted layer, as shown in Fig. 7 (b). The Cr content of remelted layer was higher than that of substrate, as shown in Fig. 7 (c). The Si and O contents of remelted layer were higher than those of substrate, as shown in Fig. 7 (d)–(e). The enrichment of O on the remelted layer was due to the oxidation during the LR process.

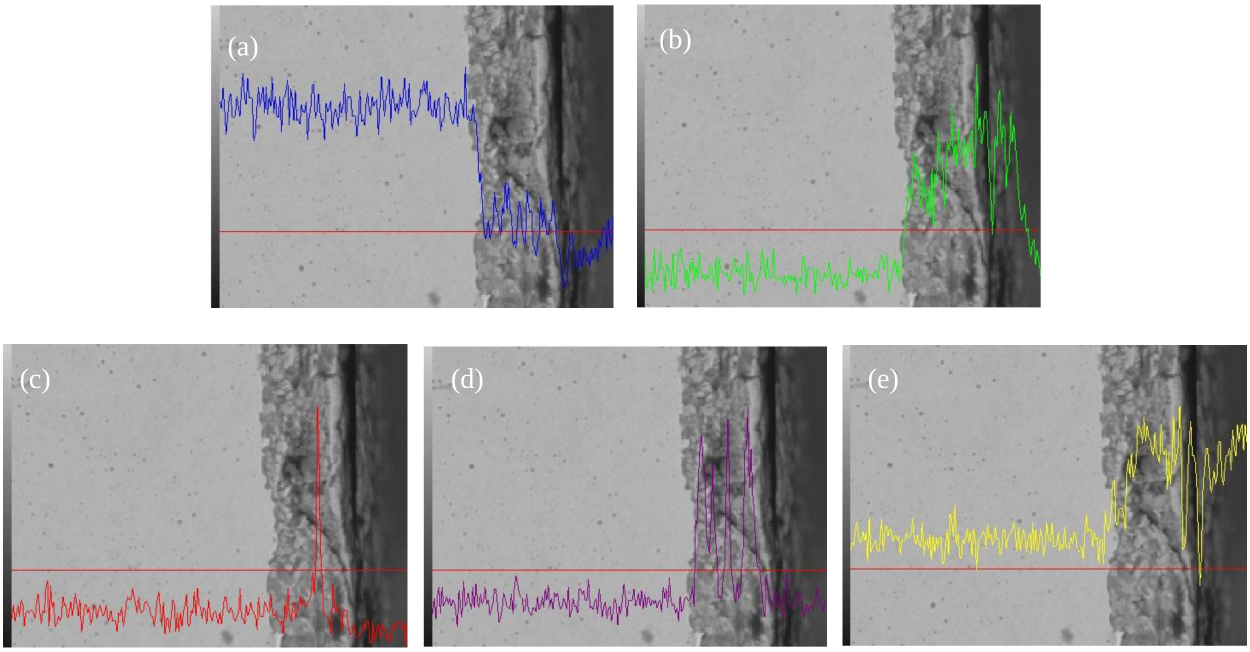

Figure 7. Line scan analysis of remelted layer cross–section at laser power of 1000 W (a) Fe content, (b) Mn content, (c) Cr content, (d) Si content and (e) O content

The line scan analysis of remelted layer cross–section in Fig. 5 (a) is shown in Fig. 8. The Fe in the substrate was obviously higher than that in the remelted layer, and decreased sharply at the diffusion interface, as shown in Fig. 8 (a). The contents of Mn, Cr, Si and O were relatively low, and they increased also sharply at the diffusion interface, which was enriched in the remelted layer, as shown in Fig. 8 (b)–(e).

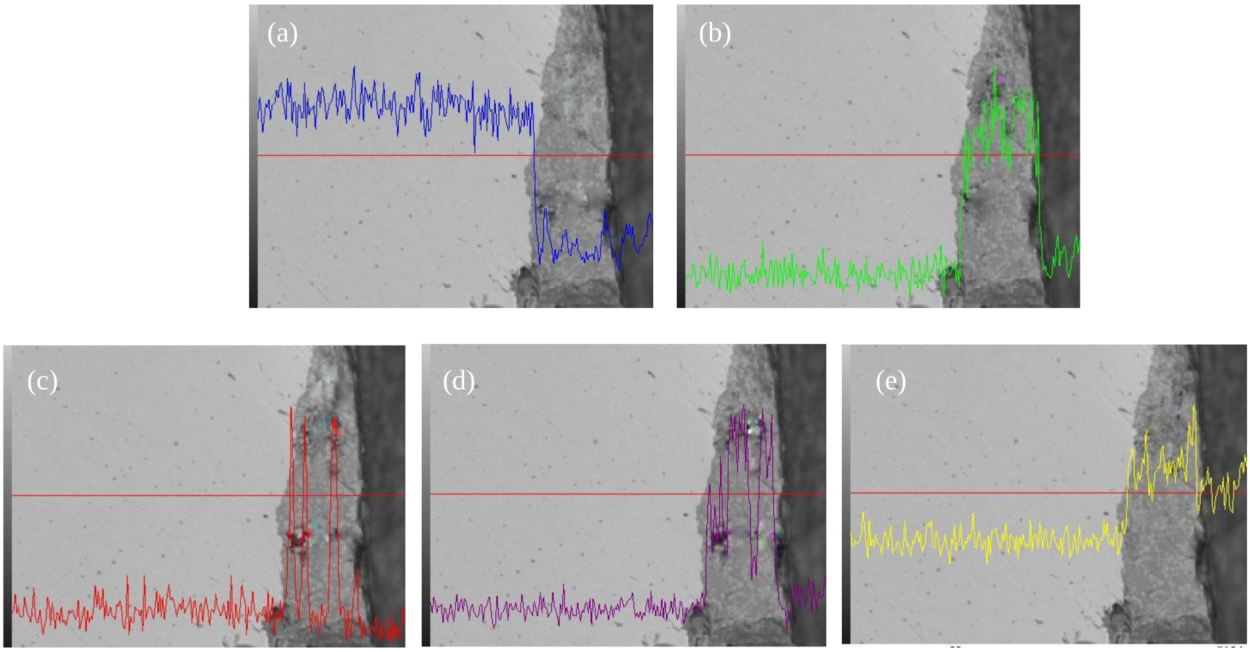

Figure 8. Line scan analysis of remelted layer cross–section at laser power of 1300 W (a) Fe content, (b) Mn content, (c) Cr content, (d) Si content, (e) O content

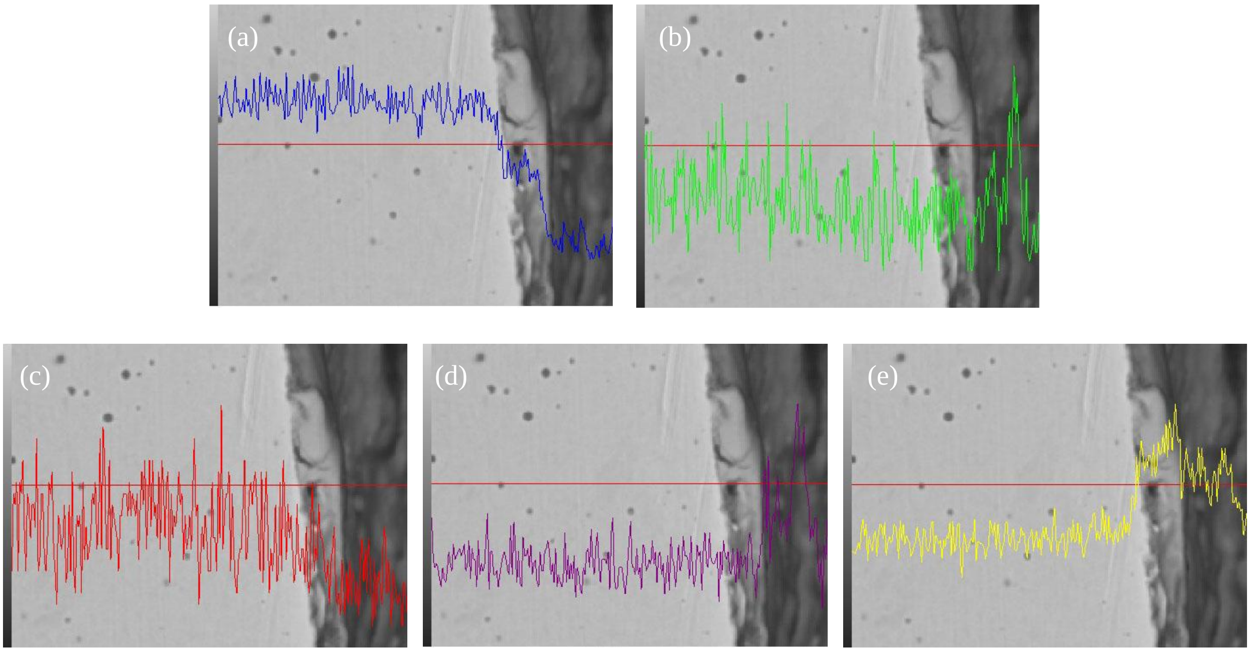

Figure 9. Line scan analysis of remelted layer cross–section at laser power of 1500 W (a) Fe content, (b) Mn content, (c) Cr content, (d) Si content, (e) O content

The line scan analysis of remelted layer cross–section in Fig. 6 (a) is shown in Fig. 9. The Fe content in the remelted layer was lower than that of substrate, which was similar to that of remelted layer at the laser powers of 1000 and 1300 W, showing an obvious two step decline in the diffusion interface, as shown in Fig. 9 (a). The Mn, Cr and Si in the remelted layer and substrate did not change significantly, the atoms–rich zones in the remelted layer disappeared, as shown in Fig. 9 (b)–(d). The O content in the remelted layer was higher than that in the substrate, as shown in Fig. 9 (e).

From the above analyses, it can be seen that the chemical elements in the substrate were diffused into the remelted layer sharply at the interface and formed the metallurgical bonding in the diffusion interface.

3.4 XRD analysis

Fig.10 shows the XRD analysis of remelted layers at different laser powers. It was found that three remelted layers were detected a broadened diffraction peaks at 50–58 $^{\circ}$, indicating that the LR process formed amorphous phases, which were mainly detected as Fe_2MoO_4, $MnFe_2O_4$, $NiMn_2O_4$ and $MnCr_2O_4$. Usually, the cooling rate of LR reached 10^6–10^8 K/s, which was rapid enough to satisfy the critical cooling rate of amorphous structure [24], inhibiting the nucleation and growth of crystal [25], and ultimately forming the amorphous phase. Among three remelted layers, there was a low intensity and sharp crystallization peak, indicating that there was a crystal phase in the remelted layer, indicating that the remelted layer was a composite structure of amorphous and crystal structure. During the LR test, although Ar was adopted to protect the molten pool, it inevitably contacted with the O in the air. The formed oxides cover the remelted layer surface inhibited the further formation of amorphous structure, so the remelted layer was composed of amorphous and crystal phases. The peak intensity decreased and broadened obviously with the laser power increasing, indicating that laser power increased the forming ability of amorphous phase.

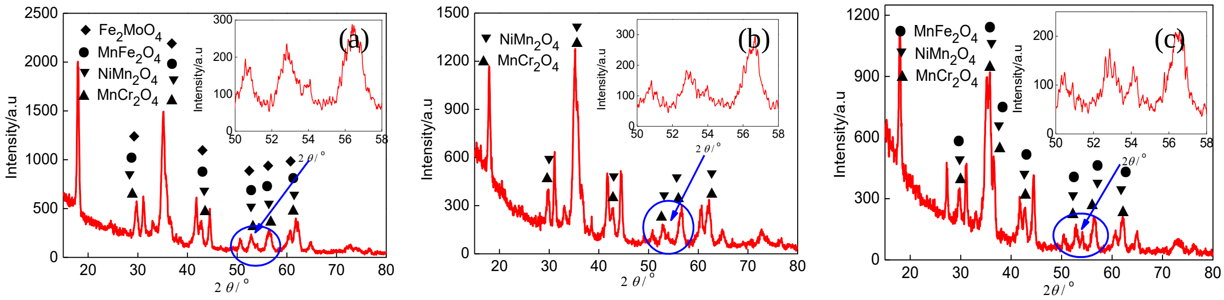

Figure 10. XRD spectra of remelted layers at different laser powers (a) 1000 W, (b) 1300 W and (c) 1500 W

3.5 DSC analysis

Fig. 11 shows DSC curves of remelted layers at a heating rate of 15 K/min. The remelted layer at the LR power of 1000 W produced a small endothermic reaction caused by glass transition in the vicinity of 41.037 ^{o}C, and with the increase of temperature, two exothermic peaks appeared at 274.23 and 423.437 ^{o}C, indicating that the remelted layer had two step of crystallization process from amorphous to crystal state. The remelted layers at the laser powers of 1300 and 1500 W formed a small endothermic peak at 61.362 and 56.372 ^{o}C. With the temperatures increasing, the relatively gentle exothermic peaks appeared at 273.562 and 273.382 °C, which marked the crystallization reaction. The three curves had a typical exothermic peak in the amorphous process, indicating that the amorphous state of crystallization process was crystallized, but the peak temperature T_p was at ~273 °C, which did not change obviously. The curves of three remelted layers had crystallized exothermic peak but no apparent glass transition temperature T_g and no obvious initial crystallization temperature, the remelted layers existed amorphous structure [26], which was consistent with the XRD analysis.

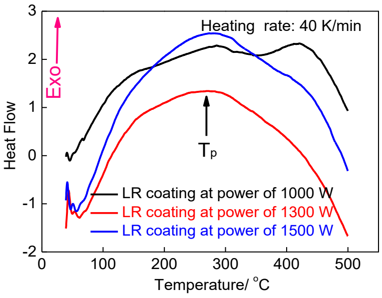

Figure 11. DSC curves of remelted layers at different laser powers

3.6 Analysis of residual stresses

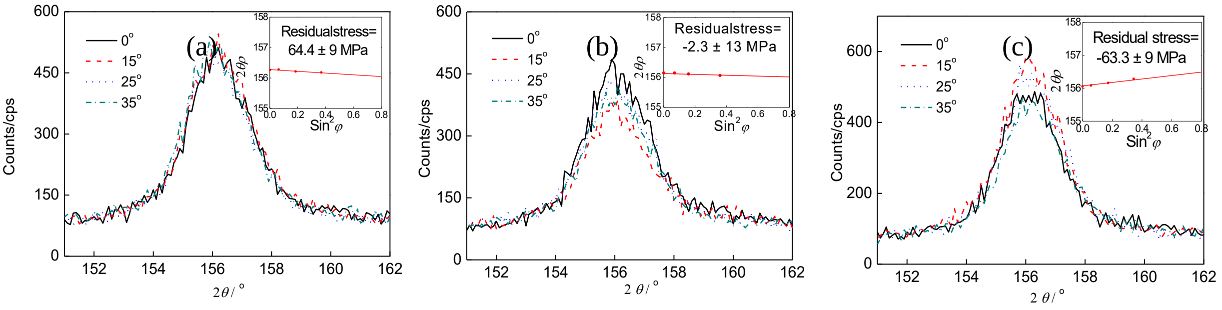

Figure 12. Residual stresses of remelted layers at different laser powers (a) 1000 W, (b) 1300 W and (c) 1500 W

Fig. 12 shows the residual stresses of remelted layers. The temperature gradient and solidification–induced shrinkage of adjacent laser melted zones generated enormous thermal stress [21]. After laser beam leaving the molten pool, the liquid metal solidified and contracted with the surrounding structure, producing deformation and structural stress. The residual stress originated from the combination of thermal stress and structural stress. From the Fig. 12 (a), it can be seen that the residual stress of remelted layer at the laser power of 1000 W was tensile stress (64.4 ± 9 MPa). The tensile residual stress in the remelted layer decreased its electrochemical corrosion resistance. The residual stress of remelted layers at laser powers of 1300 and 1500 W was –2.3 ± 13 and –63.3 ± 9 MPa, respectively, as shown in Fig. 12 (b) and (c), indicating that the residual stress of remelted layer was changed from tensile stress to compressive stress with the laser powers increasing. The compressive stress (–2.3 ± 13 MPa) formed by the remelted layer at the laser power of 1300 W was small, and the slight compressive stress was not enough to increase its electrochemical corrosion resistance. The compressive residual stress of remelted layer at laser power of 1500 W was relatively large, impelling the formation of passive film [27], which increased its electrochemical corrosion resistance.

3.7 Electrochemical corrosion

Fig. 13 shows the potentiodynamic polarization curves of remelted layers and S355 steel in 3.5% NaCl solution, showing that the polarization curves of remelted layers and S355 steel exhibited nearly identical shapes but different locations. Table 2 shows the relevant electrochemical parameters which were summarized via extrapolating the polarization curves. In general, corrosion potential (E_{corr}) represented the corrosion tendency of alloy and corrosion current density (i_{corr}) determined the corrosion rate, the higher corrosion potential and the lower corrosion current density represented the less corrosion rate and better corrosion resistance [28–31]. From Table 2, it can be seen that the corrosion potential (E_{corr}) of remelted layers shifted positively, and the corresponding corrosion current density (i_{corr}) decreased compared to those of S355 steel, indicating that LR increased its corrosion resistence. The increase of *R* from S355 steel to remelted layers was also in consistent with the analysis, which was due to a certain amount of amorphous structure and oxides naturally depositing on the remelted layer surface and forming the protective film, inhibiting its electrochemical corrosion to a certain extent [32].

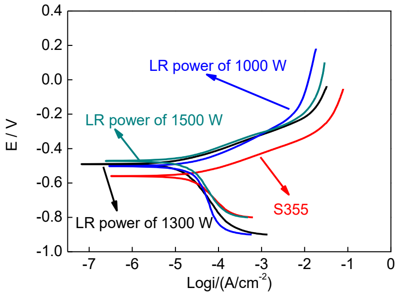

Figure 13. Polarization curves of remelted layers at different laser powers

Table 2. Polarization parameters of remelted layers and substrate in 3.5% NaCl solution

Parameter	E_{corr}/V	i_{corr}/(A/cm^{-2})	R/Ω•cm^2
Substrate	–0.56	3.072×10^{-5}	893
Laser power of 1000 W	–0.502	2.607×10^{-5}	1359
Laser power of 1300 W	–0.49	1.247×10^{-5}	2181
Laser power of 1500 W	–0.472	1.610×10^{-5}	1836

In 3.5% NaCl solution, the following reaction occurred on the cathode was

$O_2 + 2H_2O + 4e^- \rightarrow 4OH^-$ (1)

The corresponding chemical reactions on the anode were

$Fe \rightarrow Fe^{2+} + 2e^-$ (2)

$Fe^{2+} + Cl^- \rightarrow FeCl_2$ (3)

$FeCl_2 + 2H_2O \rightarrow Fe(OH)_2 + 2H^+ + 2Cl^-$ (4)

$Fe^{2+} + 4OH^- \rightarrow 2Fe(OH)_2$ (5)

Therefore, a cathodic reaction in addition to Eq.(1), i.e.

$$H^{+} + 2e^{-} \rightarrow H_2 \qquad (6)$$

The cathode branch in the polarization curves represented the hydrogen evolution reaction, while the anode branch represented the dissolution reaction of Fe [33]. The $Fe(OH)_2$ formed in Eqs. (2)–(5) precipitated gradually on S355 steel and reacted with the dissolved O to form the complex corrosion products, which were consisted of several iron oxides and hydroxide species [34], the H bubbles were released as the corrosion products [4]. The mixture of oxides after LR and corrosion products accumulated on the remelted layer, forming a protective corrosion product layer on the remelted layer, which reduced the ionic mobility between the corrosive medium and S355 steel, reducing the corrosion rate and postponed its further electrochemical corrosion.

Fig. 14 shows the impedance curves of remelted layers and S355 steel in the 3.5% NaCl solution. The AC impedance changed almost not coincided at the initial period, and subsequently, the Nyquist curves was gradually curved, and the capacitance resistance arc appeared, which represented the transfer resistance of electrochemical dissolution rate. Generally speaking, the larger the capacitance arc diameter was, the slower the corrosion reaction, and the stronger the corrosion resistance was. The impedance curves in Fig.14 were fitted with the equivalent circuit diagram based on the circuits mostly used in literature [35–38], as shown in Fig. 15 (a) and (b). Among them, Rs was solution resistance, Q_r was the film capacitance of corrosion product, R_f was the resistance of corrosion product membrane, Q_d was the capacitance of double electrode layer on the electrode surface, and R_t was the charge transfer resistance representing the impedance of the corrosion product film [39, 40]. The values of equivalent circuit elements obtained by fitting EIS date were given in Table 3. In 3.5% NaCl solution, the corrosion resistance was mainly controlled by R_t and R_f [41], the greater the R_t and R_f were, the slower the corrosion reaction was [42]. The charge transfer resistance of S355 steel and remelted layer was 1275, 1807, 1585, and 1672 $\Omega \cdot cm^2$, and the resistance of corrosion product membrane was 305.4, 234.3, and 216.3 $\Omega \cdot cm^2$, respectively, which were fitted by the electrochemical analysis software of Zsim. After the LR test, the reactance arc diameter and the charge transfer resistance of remelted alloy were greater than S355 steel, indicating that LR improved its electrochemical corrosion resistance which was consistent with the analysis results in the polarization curves, as a result, LR effectively improved the electrochemical corrosion resistance of S355 steel.

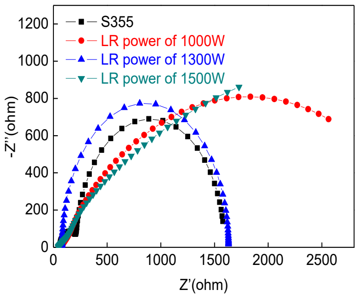

Figure 14. Impedance spectroscopy of remelted layer in 3.5% NaCl solution

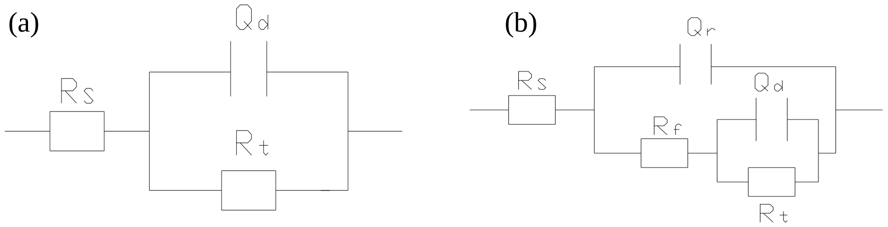

Figure 15. Electrochemical impedance spectroscopy for remelted layers in 3.5% NaCl solution (a) equivalent circuit of S355 steel and (b) equivalent circuit models of remelted layers

Table 3. Equivalent circuit parameters of remelted layers and substrate in 3.5% NaCl solution

Parameter	R_S/Ω•cm^2	Q_r/F/cm^2	R_f/Ω•cm^2	Q_d/F/cm^2	R_t /Ω•cm^2
Substrate	85.32	–	–	0.2944	1275
Laser power of 1000 W	88.34	5.632×10^{-5}	305.4	0.4210	1807
Laser power of 1300 W	61.93	3.215×10^{-5}	234.3	0.4604	1585
Laser power of 1500 W	70.21	8.894×10^{-5}	216.3	0.9392	1672

4. CONCLUSIONS

(1) There are no obvious cracks on the remelted layer surface at the laser powers of 1000 and 1300 W, while the remelted layer surface was smooth at the laser power of 1500 W, the metallurgical bonding is formed at the interface.

(2) The amorphous phases are formed in the three remelted layers, which are mainly composed of Fe_2MoO_4, $MnFe_2O_4$, $NiMn_2O_4$ and $MnCr_2O_4$, its crystallization temperature is ~273 ^{o}C, the amorphous formation capacity increased with the laser powers.

(3) The residual stress of remelted layers at the powers of 1000, 1300 and 1500 W is 64.4 ± 9, –2.3 ± 13 and –63.3 ± 9 MPa, respectively, of which the tensile stress decreases its electrochemical corrosion resistance, while the compressive stress increases its electrochemical corrosion resistance at a certain extent.

(4) The corrosion potential of remelted layers at laser powers of 1000, 1300, and 1500 W is –0.502, –0.49, and –0.472 V, respectively, and the corresponding charge transfer resistances is 1807, 1585, and 1672 Ω•cm^2 respectively, which are higher than –0.56 V and 1275 Ω•cm^2 of S355 steel, showing that LR improves the electrochemical corrosion resistance of S355 steel.

ACKNOWLEDGEMENTS
Financial support for this research by the Key Research and Development Project of Jiangsu Province (BE2016052) is gratefully acknowledged.

References

1. D. Forni, B. Chiaia and E. Cadoni, *Eng. Struct.*, 119 (2016) 164

2. Y.L. Zhou**,** J. Chen and Z.Y. Liu**,** *J. Iron. Steel Res. Int*., 20 (2013) 66
3. C.B.N. Unnisa, G.N. Devi, V. Hemapriya, S. Chitra, I.M. Chung, S.H. Kim and M. Prabakaran, *Constr. Build. Mater*., 165 (2018) 866
4. H.J. Habeeb, H.M. Luaibi, Mohammed, R.M. Dakhil, A.A.H. Kadhum, A.A. Al‑Amiery and T.S. Gaaz, *Results Phys*., 8 (2018) 1260
5. R.A.D. Medeiros‑Junior, M.G.D. Lima, P.C.D. Brito and M.H.F.D. Medeiros, *Ocean Eng.*, 103 (2015) 78
6. X.Y. Lou, P.L. Andresen and R.B. Rebak, *J. Nucl. Mater*., 499 (2018) 182
7. D.l. Cong, H. Zhou, Z.N. Ren, Z.H. Zhang, H.F. Zhang, C. Meng and C.W. Wang, *Mater. Design*, 55 (2014) 597
8. M.R. Amaya–Vazquez, J.M. Sánchez–Amaya, Z. Boukha and F.J. Botana, *Corros. Sci*., 56 (2012) 36
9. Y. Yao, X. Li, Y.Y. Wang, W. Zhao, G. Li and R.P. Liu, *J. Alloy Compd*., 583 (2014) 43
10. W.R. Osório, N. Cheung, J.E. Spinelli, K.S. Cruz and A. Garcia, *Appl. Surf. Sci*., 254 (2008) 2763
11. B. He, X. Cheng, J. Li, X.J. Tian and H.M. Wang, *Surf. Coat. Tech*., 316 (2017) 104
12. G.K. Huang, L.D. Qu, Y.Z. Lu, Y.Z. Wang, H.G. Li, Z.X. Qin and X. Lu, *Vacuum*, 153 (2018) 39
13. M.M. Pariona, V. Teleginski, K.D. Santos, E.L.R.D. Santos, A.A.D.O.C.D. Lima and R. Riva, *Mater. Charact*., 74 (2012) 64
14. E. Chikarakara, S. Naher and D. Brabazon, *Appl. Surf. Sci*., 302 (2014) 318
15. Z.H. Zhang, P.Y. Lin and L.Q. Ren, *Opt. Laser Eng*., 55 (2014) 237
16. Z.H. Zhang, P.Y. Lin, H. Zhou and L.Q. Ren, *Appl. Surf. Sci*., 276 (2013) 62
17. L.Q. Li, H.B. Xia, C.W. Tan and N.S. Ma, *J. Manuf. Process*., 32 (2018) 160
18. C.W. Wang, H. Zhou, Z.H. Zhang, Y. Zhao, P. Zhang, D.L. Cong, C. Meng and F.X. Tan, *Appl. Surf. Sci.*, 2012, 258 (22): 8732
19. B. Richter, S.X. Chen, J.D. Morrow, K. Sridharan, M. Eriten and F.E. Pfefferkorn, *J. Manuf. Process*., 32 (2018) 230
20. B. Das, A.K. Nath and P.P. Bandyopadhyay, *Ceram. Int.*, 44 (7) (2018) 7524
21. T. Simson, A. Emmel, A. Dwars and J. Bohm, *3D. Print. Addit. Manuf.*, 17 (2017) 183
22. X.Q. You, C.J. Zhang, X.F. Song, M.P. Huang and J.G. Ma, *Appl. Surf. Sci*., 253 (9) (2007) 4409
23. J.B. Yu, Y. Wang, F.F. Zhou, L. Wang and Z.Y. Pan, *Appl. Surf. Sci*., 431 (2018) 112
24. R.F. Li, Z.G. Li, J. Huang and Y.Y. Zhua, *Appl. Surf. Sci.*, 258 (2012) 7956
25. D.S. Wang, Z.J. Tian, L.D. Shen, Z.D. Liu and Y.H. Huang, *Appl. Surf. Sci*., 255 (2009) 4606
26. D.H. Zhang and D.J. Kong, *J. Alloy Compd*., 735 (2018) 1
27. Z. Sun, D.H. Zhang, B.X. Yan and D.J. Kong, *Opt. Laser Technol.*, 99 (2018) 282
28. J.D. Du, D.Y. Ding, W.L. Zhang, Z. Xu, Y.J. Gao, G.Z. Chen, W.G. Chen, X.H. You, R.Z. Chen, Y.W. Huang and J.S. Tang, *Appl. Surf. Sci*., 422 (2017) 221
29. G. Wang, C. Xing, F. Tao, P.F. Ding and Z.J. Huang, *Surf. Coat. Tech*., 305 (2016) 62
30. Z.J. Li, X.E. Wang, J.Y. Li, J. Li and H.Z. Wang, *J. Magn. Magn. Mater*., 442 (2017) 62
31. J.S. Wu, K. Pang, D.D. Peng, J.W. Wu, Y.X. Bao and X.G. Li, *Int. J. Electrochem. Sci*., 12 (2017) 1216
32. J.L. Yang, Y.F. Lu, Z.H. Guo, J.f. Gu and C.X. Gu, *Corros. Sci*., 130 (2018) 64
33. M. Mobin and R. Aslam, *Process Saf. Environ*., 114 (2018) 279
34. A. Zeino, I. Abdulazeez, M. Khaled, M.W. Jawich and I.B. Obot, *J. Mol. Liq*., 250 (2018) 50
35. L. Vrsalovic, S. Gudic, D. Gracic, I. Smoljko, I. Ivanic, M. Kliskic and E.E. Oguzie, *Int. J. Electrochem. Sci*., 13 (2018) 2102
36. L.Y. Zhang, S.H. Zhang, Y. He, R.R. Yang, L. Ma, Y.Q. Xia and Z. He, *Int. J. Electrochem. Sci*., 13 (2018) 2136
37. Z.X. Yang, B. Kan, J.X. Li, Y.J. Su and L.J. Qiao, *J. Electroanal. Chem*., 822 (2018) 123
38. Q.S. Li, J.H. Wang, X.T. Xing and W.B. Hu, *Bioelectrochemistry.* 122 (2018) 40
39. M. Bagherzadeh and F. Jaberinia, *J. Alloy Compd*., 750 (2018) 677

40. H. Nady, M.M. El–Rabiei and M. Samy, *J. Petrol. Sci. Eng.*, 26 (2017) 79
41. M.X. Zhang, H.X. Liu, S.K. Karn, J.Z. Duan, F. Guan, X.F. Zhai, S.J. Zhao, K. Li and B.R. Hou, *Int. J. Electrochem. Sci.*, 12 (2017) 2315
42. X.D. Zhang, X.Q. Du, C. Cai and Z. Zhang, *Int. J. Electrochem. Sci.*, 12 (2017) 2412